Tracing molecular stratification within an edge-on protoplanetary disk

D. Ruíz-Rodríguez, J. Kastner, P. Hily-Blant, T. Forveille

A&A 646, A59 (2021)
https://doi.org/10.1051/0004-6361/202038209

Astronomy & Astrophysics

Tracing molecular stratification within an edge-on protoplanetary disk

D. Ruíz-Rodríguez[1,2], J. Kastner[2], P. Hily-Blant[3], and T. Forveille[3]

[1] National Radio Astronomy Observatory, 520 Edgemont Rd., Charlottesville, VA 22903, USA
e-mail: druiz@nrao.edu
[2] Chester F. Carlson Center for Imaging Science, School of Physics & Astronomy, and Laboratory for Multiwavelength Astrophysics, Rochester Institute of Technology, 54 Lomb Memorial Drive, Rochester NY 14623 USA
[3] Université Grenoble Alpes, CNRS, IPAG, 38000 Grenoble, France

Received 20 April 2020 / Accepted 18 December 2020

ABSTRACT

High-resolution observations of edge-on protoplanetary disks in emission from molecular species that sample different critical densities and formation pathways offer the opportunity to trace the vertical chemical and physical structures of protoplanetary disks. Among the problems that can be addressed is the origin and significance of the bright CN emission that is a ubiquitous feature of disks. Based on analysis of subarcsecond-resolution Atacama Large Millimeter Array archival data for the edge-on Flying Saucer disk (2MASS J16281370-2431391), we establish the vertical and radial differentiation of the CN emitting regions of the disk with respect to those of ^{12}CO and CS, and we model the physical disk conditions from which the CN emission arises. We demonstrate that the ^{12}CO (2–1), CN (2–1), and CS J = 5–4 emitting regions of the disk decrease in scale height above the midplane, such that ^{12}CO, CN, and CS trace layers of increasing density and decreasing temperature. We find that at radii >100 au from the central star, CN emission predominantly arises from intermediate layers, while in the inner region of the disk CN appears to arise from layers closer to the midplane. We investigate the physical conditions of the disk within the CN emitting regions, as well as the ranges of CN excitation temperature and column density, via RADEX non-local thermodynamic equilibrium (non-LTE) modeling of the three brightest CN hyperfine lines. Near the disk midplane, where we derive densities of $n_{\rm H_2} \sim 10^7$ cm^{-3} at relatively low $T_{\rm kin}$ (∼12 K), we find that CN is thermalized, while sub-thermal, non-LTE conditions appear to obtain CN emission from higher (intermediate) disk layers. We consider whether and how the particular spatial location and excitation conditions of CN emission from the Flying Saucer can be related to CN production that is governed, radially and vertically, by the degree of irradiation of the flared disk by X-rays and UV photons from the central star.

Key words. submillimeter: planetary systems – stars: pre-main sequence – astrochemistry

1. Introduction

Detailed chemical studies of dusty circumstellar (protoplanetary) disks orbiting young stars represent necessary steps toward understanding how exoplanets and exocomets obtain their chemical inventories. The unprecedented combination of sensitivity and spatial and spectral resolution afforded by the Atacama Large Millimeter Array (ALMA) is now enabling such investigations (e.g., Qi et al. 2013, 2019; Öberg et al. 2015; Guzmán et al. 2017; Hily-Blant et al. 2017; Bergner et al. 2018; Kastner et al. 2018; Semenov et al. 2018; Öberg & Wordsworth 2019).

Among the problems that can be addressed via spatially resolved ALMA studies of protoplanetary disk chemistry is the origin and significance of the bright CN emission that is a ubiquitous feature of disks (e.g., Kastner et al. 1997, 2008, 2014; Thi et al. 2004; Sacco et al. 2014; Guilloteau et al. 2014). Different astrochemical models of protoplanetary disk CN production, most of which attempt to account for the influence of high-energy stellar irradiation, have made a variety of predictions as to CN abundances and locations (e.g., Lepp & Dalgarno 1996; Stäuber et al. 2005; Chapillon et al. 2012; Cleeves et al. 2013; Cazzoletti et al. 2018). In particular, most models predict that CN is mostly produced within disk surface layers via UV irradiation (either through photodissociation of HCN or via vibrational excitation of H_2; Cazzoletti et al. 2018; Visser et al. 2018). However, the low CN kinetic temperatures inferred from observations ($T \leq 25$ K; e.g., Kastner et al. 2014; Teague et al. 2016; Hily-Blant et al. 2017) suggest that disk CN production may be driven by more deeply penetrating X-ray radiation from the central T Tauri stars (Kastner et al. 2014).

Confirming or ruling out whether CN can be formed deep within protoplanetary disks would have several interesting implications. Foremost, it would contribute to establishing whether CN is a photodissociation product of HCN or if it is formed via other channels, such as reactions of N with C_2H (Cazzoletti et al. 2018). This, in turn, would help to constrain the physical and chemical processes that took place during the formation of the various isotopic reservoirs of nitrogen present in the Solar System (Guzmán et al. 2017; Hily-Blant et al. 2017, 2019).

Despite the status of CN as a signature chemical tracer within disks – and the foregoing open questions concerning its production and its utility as a tracer of UV irradiation and nitrogen isotopic ratios – the only ALMA CN images of disks published thus far have been those for the nearly pole-on TW Hya and a handful of moderately inclined disks (Teague et al. 2016; Hily-Blant et al. 2017; van Terwisga et al. 2019; Teague & Loomis 2020). The ring-like CN emission morphologies revealed by

Table 1. Detected CN (N = 2–1) HF transitions.

HF component [(a)]	Transition	ν [GHz]	A_{ul}	g_u	Relative intensities [(b)]
A	$J = 5/2 \rightarrow 3/2$, $F = 5/2 \rightarrow 3/2$	226.8741908	9.62×10^{-5}	6	0.1805
B	$J = 5/2 \rightarrow 3/2$, $F = 7/2 \rightarrow 5/2$	226.8747813	1.14×10^{-4}	8	0.2860
C	$J = 5/2 \rightarrow 3/2$, $F = 3/2 \rightarrow 1/2$	226.8758960	8.59×10^{-5}	4	0.1074
D	$J = 5/2 \rightarrow 3/2$, $F = 3/2 \rightarrow 3/2$	226.8874202	2.73×10^{-5}	4	0.0342
E	$J = 5/2 \rightarrow 3/2$, $F = 5/2 \rightarrow 5/2$	226.8921280	1.81×10^{-5}	6	0.0340

Notes. [(a)]CN (2–1) has 19 HF components. We list here the five brightest (hence well-detected) HF components within the observed bandpass, referred to throughout this paper as A to E. Molecular data from Skatrud et al. (1983). [(b)]Theoretical relative intensities under LTE conditions of the five brightest HF transitions of CN within the bandwidth, adapted from Table 2 in Punzi et al. (2015).

these images motivated recent model calculations by Cazzoletti et al. (2018), and the observed morphologies are indeed well reproduced by these simulations. However, the degeneracy inherent to low-inclination viewing geometries has left constraints on the scale height of CN emission entirely in the realm of the aforementioned temperature-based inferences.

To more directly investigate the vertical distribution of CN molecules within protoplanetary disks, we have exploited archival ALMA data obtained for the nearly edge-on Flying Saucer disk (2MASS J16281370−2431391). The CN data analyzed here were obtained as part of the comprehensive study of the vertical and radial physical (density and temperature) structure of that disk carried out by Guilloteau et al. (2016) and, subsequently, by Dutrey et al. (2017).

The Flying Saucer system consists of a 0.57 $M_\odot$ young stellar object surrounded by a nearly edge-on disk ($i \approx 87°$) of mass 3.5×10^{-5} $M_\odot$. Its distance is estimated at ~120 pc (Loinard et al. 2008). As no parallax is available for the Flying Saucer system in the second *Gaia* data release (DR2; Gaia Collaboration 2018), we adopted this distance for all calculations in this paper. The aforementioned ALMA observations revealed the ^{12}CO J = 2–1 emission lying well above and below the disk plane, arising from upper and lower layers, extending to disk radii of at least 330 au. By contrast, the CS J = 5–4 molecular emission is confined toward the midplane and extends to ~300 au in radius (Dutrey et al. 2017). Contrary to the radial extension of the CS and ^{12}CO (hereafter CO) emission, the dust continuum is limited to a more compact region with a radius of 190 au and, similarly to the CS emission, is confined toward the midplane, where the dust temperature is remarkably low (T_{Dust} ~ 5–8 K at 100 au; Guilloteau et al. 2016). Modeling of continuum and near-IR emission suggests that the disk is in an advanced state of dust settling, with scale heights of 22.5 ± 1.5 au for small grains (~1 μm) and 12.7 ± 0.3 au for large grains (~1 mm) at 100 au (Grosso et al. 2003).

Indeed, CO, CS, and 242 GHz continuum emission reveal a vertical stratification of the dust and gas in the system (Dutrey et al. 2017). These stratified disk density and temperature tracers hence potentially afford a direct means to constrain CN production pathways under different thermal and density conditions. To exploit this potential, we have analyzed the CN emission line data for the Flying Saucer disk that were obtained during the same ALMA observations that yielded the maps of CO, CS, and continuum (Dutrey et al. 2017). Sections 2 and 3 present details of the observations as well as the CS, CN, and CO molecular emission line maps resulting from our reprocessing of the archival ALMA data. In Sect. 3, we present an analysis of the disk's vertical intensity distributions and the CN emission line profiles, together with the derivation of the disk's physical parameters. Section 4 presents a discussion of the disk structure, CN abundances, and potential triggers of CN production in the disk at different scale heights and radii.

2. Observations

The CN N = 2–1, CS J = 5–4, and CO J = 2–1 observations of the Flying Saucer presented in this work were obtained on May 17 and 18, 2015, as part of the Cycle 2 program 2013.1.00387.S (PI: Guilloteau). Using 37 12-meter antennas, the range of unprojected baseline lengths was from 15 to 560 m, and the total observation time was ~55 min. As previously noted, a detailed description and analysis of the continuum, CO, and CS data was presented in Guilloteau et al. (2016) and Dutrey et al. (2017).

Here, we reprocessed the ALMA data. To that end, the ALMA visibility data were edited, calibrated, and imaged using the pipeline version r39732 in CASA 4.2.2. To image the data, we used the TCLEAN algorithm. We performed self-calibration on the source continuum emission with three rounds of phase calibration. To achieve a good balance between sensitivity and angular resolution, the Briggs weighting parameter R was set to 0.5 for the continuum map and spectral line image cubes. For the continuum map, this yields a synthesized beam of 0.53″ × 0.52″ at PA −65.1°. The peak 242 GHz continuum flux is 8.5 mJy beam^{-1}, and the root mean square (rms) is 0.2 mJy beam^{-1}. Given the relatively weak continuum emission, continuum subtraction should not remove significant line flux (Weaver et al. 2018). For the lines of interest, we then subtracted the continuum emission by fitting a first-order polynomial to the continuum in the uv-plane and produced spectral data cubes with 0.06 km s^{-1} velocity resolution. The image cubes were constructed on a 256 × 256 pixel grid with 0.1″ pixel size. For CS, the resulting rms was ~2 mJy beam^{-1} (~0.10 K) with a synthesized beam of 0.53″ × 0.51″ (~60 au) at PA −57.8°. For CO, the rms was ~2.5 mJy beam^{-1} (~0.14 K) with a synthesized beam of 0.56″ × 0.54″ (~65 au) at PA −63.4°. For CN, the rms was ~2 mJy beam^{-1} (~0.11 K) with a synthesized beam of 0.57″ × 0.55″ (~65 au) at PA −55.0°. In the last case, the five brightest (of the 19 total) CN (2–1) hyperfine (HF) components were detected within the frequency range covered by these observations, 226.87–226.89 GHz. These CN HF lines at 226.8741908, 226.8747813, 226.8758960, 226.8874202, and 226.8921280 GHz are labeled as "A", "B", "C", "D", and "E" in Table 1, respectively.

We constructed moment 0 maps from each of the three spectral line data cubes (Sect. 3.1), including a map that merges CN components A-E, by clipping the signal at $<1\sigma_{rms}$. The total continuum flux is 37.4 ± 0.88 mJy at 242 GHz, which is in good

agreement with the 35 mJy with ∼7% calibration uncertainty obtained by Dutrey et al. (2017) from the same ALMA dataset. The integrated emission line intensities over the entire emitting region are 1.60 ± 0.05 Jy km s^{-1}, 3.90 ± 0.12 Jy km s^{-1}, and 1.80 ± 0.16 Jy km s^{-1} for CS, CN, and CO, respectively. These flux uncertainties were estimated with the sum in quadrature of $\lesssim$10% flux and rms (per the ALMA Cycle 2 Technical Handbook[1]). The CN line flux is consistent with that obtained by Reboussin et al. (2015), 3.4 ± 0.5 Jy km s^{-1}, with the IRAM 30-m telescope.

3. Results

3.1. Integrated intensity maps and scale heights

Figure 1 shows the integrated intensity (moment 0) maps of the Flying Saucer disk in the CS J = 5–4, CN N = 2–1, and CO J = 2–1 emission lines together with the 242 GHz continuum emission. Figure 1 also displays the CS, CN, and CO radial intensity profiles along the midplane of the nearly edge-on disk in the images as well as representative vertical intensity profiles extracted along a cut at 170 au from the central source. In the CN moment 0 image and radial intensity profile, the emission displays a deficit toward the central star, suggestive of an edge-on ring structure. The CS moment 0 map and its radial profile display a very similar double-peaked morphology (see also Dutrey et al. 2017). The western regions of the CO moment 0 image are adversely affected by contaminating background emission (Dutrey et al. 2017), such that the radial profile of CO emission is difficult to interpret. Emission from both CN and CS peaks at radii of ∼70 au.

From the radial profiles, we find that the bulk of the CS line emission (>75%) originates within approximately ∼200 au of the central source and has a total extension of ∼300 au, as also reported by Dutrey et al. (2017). By contrast, the CN emitting region extends to at least 360 au, well beyond the maximum radius of CS emission. Moreover, at distances greater than 180 au, where the CO emission intensity in the midplane drops abruptly on the (uncontaminated) eastern side of the disk, the CN emission in the moment 0 map remains bright and confined closer to the midplane.

To describe the molecular emission structure of the disk, we estimated the characteristic vertical disk height of CS, CN, and CO emission (H_r) at various radii from 60 to ∼300 au. These vertical profiles were extracted along a position angle (PA) of ∼3.6° measured east from north (Dutrey et al. 2017). For the continuum, CS, and CN, which are marginally resolved, we used the full width at half maxima (FWHMs) of Gaussian fits to the observed vertical profiles to quantify H_r.

Assuming that the characteristic emission height at a given radius r is similar on the western and eastern sides of the disk, the estimated FWHM values are averaged. Figures 1a and b illustrate representative profiles along vertical cuts at a radius of 170 au on each side, verifying their similarity. To obtain H_r, we then deconvolved the beamwidth ($\theta_{\rm FWHM}$) from the resulting FWHM:

$$H_r = \frac{\left(\sqrt{FWHM^2 - \theta^2_{FWHM}}\right)}{2\sqrt{2\ln 2}}. \quad (1)$$

It should be noted that the resulting characteristic emission height H_r is likely directly related to the vertical scale height of the molecular species in question. However, given the caveats – in particular, that the emission from a given species only directly traces the disk density structure and abundance gradients if optically thin – it is important to not equate the results for H_r to disk scale height measurements.

[1] https://almascience.eso.org/documents-and-tools/cycle-2/alma-technical-handbook/

Table 2. Results of vertical profile analysis.

Data	Radius [au]	$FWHM^{(a)}$ [au]	Beam [au]	$H_r{}^{(b)}$ [au]
242 GHz		99.4 ± 0.3	63.8	32.0 ± 1.2
CS		129.5 ± 0.9	63.3	48.0 ± 0.7
CN	60	154.9 ± 0.7	68.2	59.1 ± 0.6
CO		193.2 ± 1.7	67.5	76.9 ± 0.9
242 GHz		99.7 ± 0.3	63.8	32.3 ± 1.1
CS		143.5 ± 1.8	63.3	54.7 ± 0.9
CN	100	169.1 ± 1.5	68.2	65.7 ± 0.8
CO		127.6 ± 3.0$^{(c)}$	67.5	107.2 ± 1.6
242 GHz		103.4 ± 0.7	63.8	38.1 ± 1.2
CS		159.0 ± 4.8	63.3	61.9 ± 2.3
CN	180	205.7 ± 4.5	68.2	82.4 ± 2.0
CO		123.6 ± 3.9$^{(c)}$	67.5	138.3± 2.2

Notes. $^{(a)}$Parameters obtained from Gaussian fit. For details, see Sect. 3.1. $^{(b)}$Characteristic emission height obtained after deconvolving FWHM from beam size. $^{(c)}$Multi-Gaussian fitting performed; see text.

In the specific case of CO emission at $r \geq 100$, whose vertical extent is clearly larger than CS and CO, the shapes of the vertical profiles change considerably as a function of r, as a result of CO freeze-out processes and self-absorption by colder gas along the disk midplane (Dutrey et al. 2017). These effects are manifested in the form of a lack of CO emission from the midplane, generating double-peaked vertical intensity profiles (see Fig. 1c). Hence, the disk scale height cannot be characterized by the above approximation (Eq. (1)). Instead, the height of the disk surface can be estimated by accounting for the resulting double-peaked vertical profiles (see Fig. 1c), whose peak positions (μ) increase as disk radius increases in a flared disk. Thus, the upper and lower disk layers, also labeled as H_r, can be computed from

$$H_r = \frac{\left(\sqrt{FWHM^2 - \theta^2_{FWHM}}\right)}{2\sqrt{2\ln 2}} + |\mu|, \quad (2)$$

with the FWHM defined as

$$FWHM = 2\sqrt{2\ln 2}\sigma. \quad (3)$$

Here, μ and σ are the peak position and the width of the Gaussian fit, respectively, and μ accounts for an offset in the peak of the distribution. We then adopted the average of these (upper and lower) H_r values. Bearing in mind that CO is contaminated by background emission from extended molecular clouds at velocities around ∼1.8 km s^{-1} and in the range 6–7 km s^{-1} (Guilloteau et al. 2016), we only analyzed vertical profiles from the least contaminated region (i.e., the eastern side of the disk). Overall, H_r values were only measured over the area where the signal is >3σ. Table 2 displays the resulting H_r values at 60, 100, and 200 au for the CS, CN, and CO molecular lines.

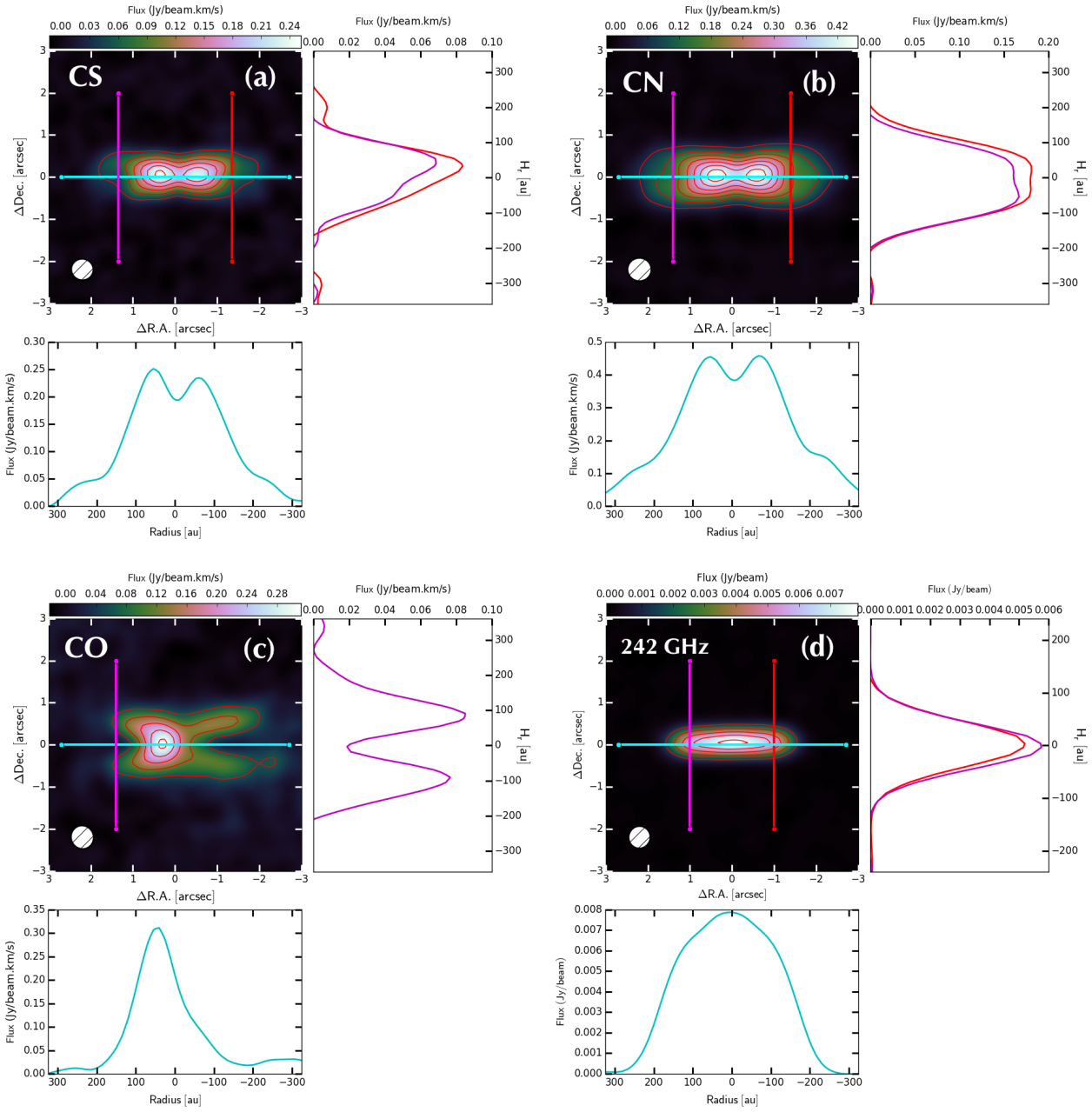

Fig. 1. Integrated emission and dust continuum images at 242 GHz of the nearly edge-on Flying Saucer disk. *Panel a*: integrated emission map of CS from −0.9 to 8.6 km s^{-1} with contours showing 10, 20, 30, 40, 50, and 60σ emission (σ = 55 mJy beam^{-1} km s^{-1}); the 0.53″ × 0.51″ at PA −57.8° beam is indicated in the bottom left corner. *Panel b*: integrated emission map of CN from 0.8 to 10.4 km s^{-1} with contours showing 10, 20, 30, 40, 50, 60, 70, and 80 σ emission (σ = 60 mJy beam^{-1} km s^{-1}) and a 0.57″ × 0.55″ at PA −55.0° beam. *Panel c*: integrated emission map of CO from −0.9 to 8.6 km s^{-1} with contours showing 10, 20, 30, and 40σ emission (σ = 90 mJy beam^{-1} km s^{-1}) and a 0.56″ × 0.54″ at PA −63.4° beam. *Panel d*: ALMA 1.236 mm dust continuum image (natural weighting) with a 0.64″ × 0.60″ at PA −56° beam. At the bottom of each panel, the radial intensity profiles of the integrated CS, CN, and CO emissions and 242 GHz continuum are shown. The radial profiles are extracted along a cut through the disk midplane (PA = 3°) and displayed by cyan lines in each image. Similarly, to the right of each panel, the representative vertical intensity profiles of the integrated CS, CN, and CO emissions are shown. The vertical profiles are extracted along a cut at a radius of 170 au for CS, CN, and CO, and at 120 au for the 242 GHz continuum. (See Sect. 3.1.)

The tabulated uncertainties only reflect the formal errors on the Gaussian fits to the intensity profiles[2].

In Fig. 2, we illustrate H_r as a function of radius in the disk. It is immediately apparent that the peak emission from the three molecular species is stratified, with CO, CN, and CS lying increasingly close to the disk midplane (as traced by the dust continuum emission). We discuss these results in more detail in Sect. 4.1.

3.2. CN emission

Figure 3 presents channel maps of CN emission, where the A, B, and C HF emission components, indicated by the circles, are spatially resolved and appear according to their

[2] We find very similar values of H_r for CS and CN if we adopt the double-Gaussian fitting approach used for CO, i.e., if we use Eq. (2) rather than Eq. (1) to define H_r.

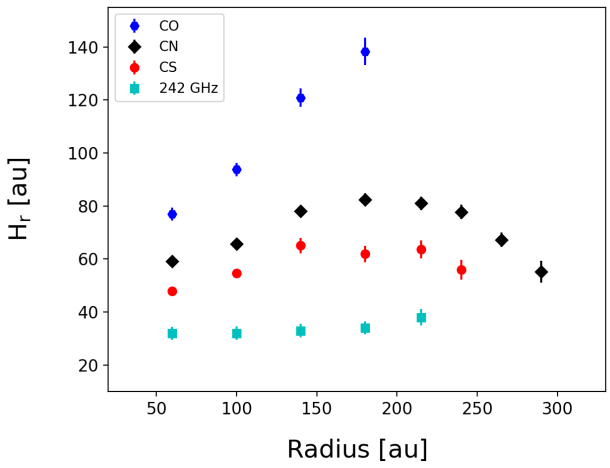

Fig. 2. Vertical scale heights estimated at various radii from the CO (blue hexagons), CN (black diamonds), CS (red dots), and 242 GHz continuum (cyan squares) integrated emission images. The H_r values are only measured over the area where the signal is >3σ, and error bars display the standard error of the mean.

frequency-equivalent velocity. These CN channel maps were generated with central velocities from +0.8 to +6.6 km s^{-1} with respect to the brightest HF component (labeled B in Table 1).

As is the case for the CO emission from the Flying Saucer (Dutrey et al. 2017), these CN channel maps reveal the vertical structure of a flared, gaseous disk, with blue-shifted material to the west (W) and red-shifted material to the east (E). However, in these CN channel maps, the HF splitting of the CN molecule visually distorts the typical emission expected from Keplerian rotation seen at high inclinations. This visual distortion is caused by the overlapping of the HF components in velocity space at different locations in the disk, as is apparent from the position-velocity (PV) diagram presented in Fig. 4. Furthermore, the disk shows nearly symmetric CN emission, with an emission deficit in the midplane at radii between ~80 and 200 au. The CN emission from this region seems to trace upper and lower surfaces, which, in some iso-velocity curves, reconnect at the outer region of the disk, forming an outer wall. This emission feature – highlighted by the B component – is most evident in channels at projected velocities of ≈2.4 and ±0.2 km s^{-1} and 5.0 and ±0.2 km s^{-1} (≈1.5 km s^{-1} from the systemic velocity). A similar pattern is detected in the weaker components, D and E, which fall outside the range plotted in Fig. 3 (see Figs. A.1 and A.2), and in the channel maps of CS emission (Fig. B.1).

3.2.1. Position-velocity diagram

Figure 4 displays a PV diagram centered on the three brightest CN (2–1) HF components (A, B, and C; Table 1), obtained from a cut along the major axis of the disk (i.e., PA ~ 93.5 deg). In these as well as the fainter HF components (D and E; see Appendix A), the PV diagram reveals a disk consistent with Keplerian rotation – with red-shifted emission to the east and blue-shifted to the west – as is the case for the CO and CS lines (Dutrey et al. 2017). Taking the brightest HF line (B component) as the reference frame, the PV diagram is well reproduced by a Keplerian rotation profile in a geometrically thin disk with an inclination of 87 ± 1.0 deg., a central mass of 0.60 ± 0.02 $M_\odot$, and a kinematic local standard of rest (KLSR) velocity ($v_{\rm LSRK}$) of 3.70 ± 0.5 km s^{-1}, assuming a distance of 120 pc. These values are in good agreement with the previous estimate of 0.58 ± 0.01 $M_\odot$ obtained from a model of the disk CS emission by Dutrey et al. (2017).

3.2.2. CN line profiles and parameters

The CN HF transitions are well resolved at radii larger than 210 au, on both the eastern and western sides of the disk. Figure 5 presents the spectra extracted from ellipse-shaped apertures, centered on regions spatially represented by the cyan ellipses drawn in Fig. 4, for which the HF splitting is well resolved. We used Gaussian fits to these line profiles to determine linewidths and relative integrated intensities of the five HF components, A to E. The results for components A to C are shown in Fig. 5 for the western and eastern sides, and results for all five components are summarized in Table 3. Under optically thin local thermodynamic equilibrium (LTE) conditions, the ratio of the intensity of the HF components relative to the brightest component (A/B, C/B, D/B, and E/B) range between 0.1 and 0.7; the theoretical intensity ratios of the HF components are listed in Table 3. Under optically thick conditions and for a uniform excitation temperature, the lines saturate, reaching equal intensities in the limit of very large optical depths.

At radii >210 au, the A, B, C, D, and E components are, at most, marginally optically thick, as determined by the measured HF transition ratios shown in Table 3. We also note that the estimated HF transition ratios within 210 au (not listed) trend toward 1.0, suggesting the emission is becoming optically thicker. Overall, the D and E components in the CN spectrum are smeared out toward the central source, becoming unresolvable, while the emission in A and C are boosted to intensities nearly comparable to the B component until those components (A+B+C) are blended together into a broad profile centered close to the systemic velocity (3.70 km s^{-1}).

3.3. CN column densities

The analysis of Sect. 3.2.2 provides indications of CN line opacities but does not address the key physical conditions that give rise to the emission, in particular, CN column densities[3] ($N_{\rm CN}$) and excitation temperatures ($T_{\rm ex}$). To ascertain the range of these and other parameters (e.g., optical depth, τ, and H_2 number density, n_{H_2}) as functions of position within the disk, we modeled the CN HF line structure using a grid-based parameter exploration approach that exploits the non-LTE radiative transfer code RADEX under the so-called large velocity gradient (LVG) framework (van der Tak et al. 2007). RADEX uses an escape probability formalism, with five parameters as inputs: n_{H_2}, $N_{\rm CN}$, kinetic temperature ($T_{\rm kin}$), background temperature, and linewidth. To explore a range of thermal parameters consistent with previous studies (e.g., Guilloteau et al. 2016; Dutrey et al. 2017), we constructed a 3D grid consisting of 21 H_2 density values in the range n_{H_2} = 10^4–10^9 cm^{-3}, 21 values of CN column density in the range $N_{\rm CN}$ = 10^{11}–10^{17} cm^{-2}, and 51 values of $T_{\rm kin}$ from 5 to 60 K. As part of the fitting process (see below), we up-sampled these RADEX 3D-grid models by interpolating between grid points to increase the resolution of the parameter space explored. The FWHM linewidth of all three HF components was held fixed at 0.4 km s^{-1}, which is the average of the individual linewidths derived in Sect. 3.2.2. For the background temperature, we adopted 2.73 K. For CN emission, RADEX then

[3] It must be noted that the $N_{\rm CN}$ values derived here represent line-of-sight CN column densities, as opposed to CN column densities measured vertically through the disk.

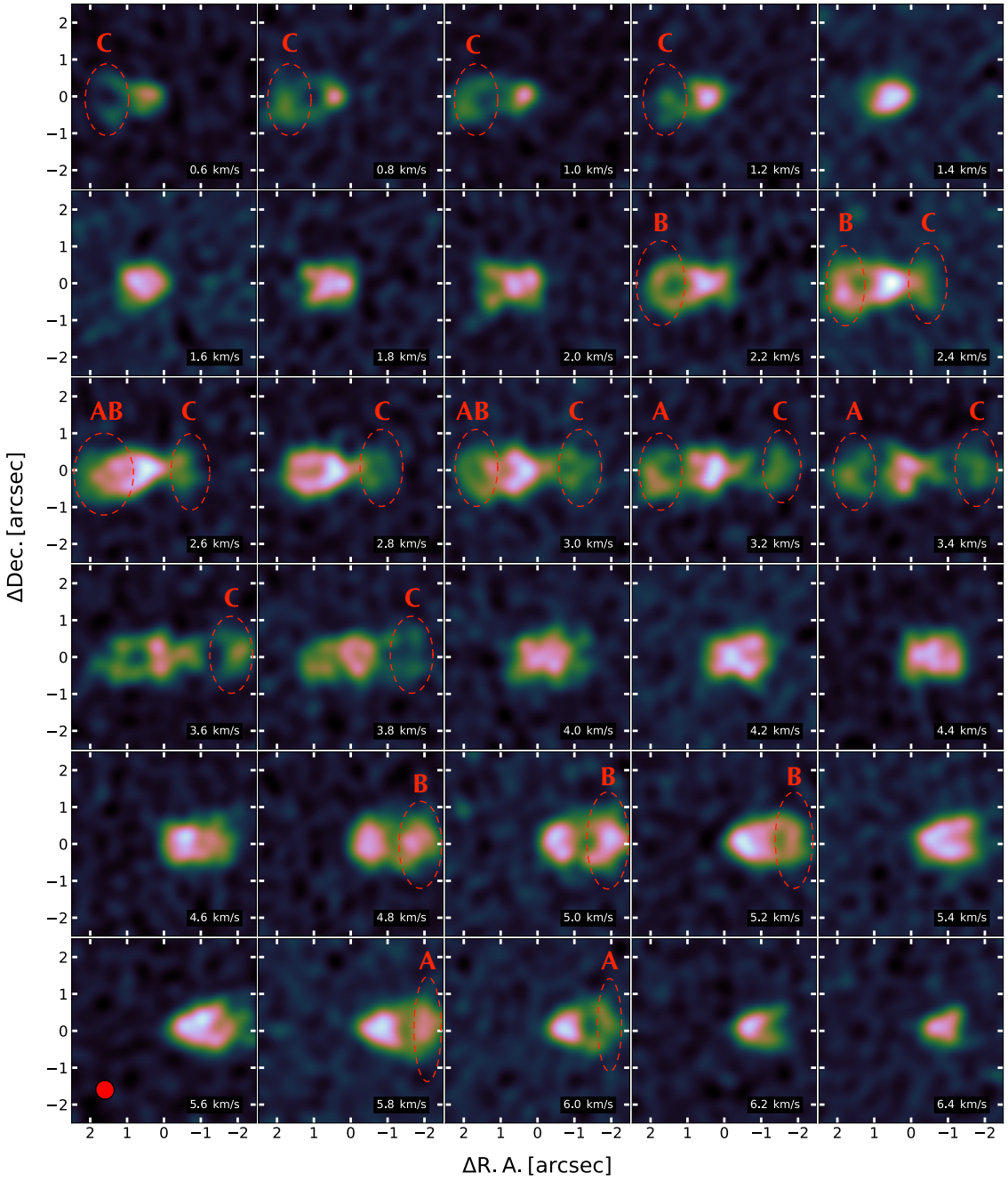

Fig. 3. Channel maps of the CN emission in the Flying Saucer from 0.60 to 6.40 km s^{-1} with the velocity labels referring to the B component. The spectral resolution is 0.2 km s^{-1} and the rms per channel is 14 mJy beam^{-1}. The synthesized beam size is represented in the *lower left panel*. The frequency range covers the A, B, and C HF components, which are $J = 5/2 \rightarrow 3/2$ and $F = 5/2 \rightarrow 3/2$, $J = 5/2 \rightarrow 3/2$ and $F = 7/2 \rightarrow 5/2$, and $J = 5/2 \rightarrow 3/2$ and $F = 3/2 \rightarrow 1/2$, respectively, and are listed in Table 1.

predicts T_{ex} and τ values for the A, B, and C components from each set of these input parameters (T_{kin}, n_{H_2}, linewidth, N_{CN}) using collision rates from Hily-Blant et al. (2013). Since RADEX does not treat line overlaps, we restricted the spectral modeling to disk regions where these CN HF structures are well resolved (see below).

To perform HF line fitting covering the full spectral range of the A+B+C components, we used a forward-fitting approach that is built into the PySpecKit Python package (Ginsburg & Mirocha 2011). For each grid point (i.e., combination of T_{kin}, n_{H_2}, and N_{CN}), the RADEX-computed T_{ex} and τ parameters were used to generate synthetic line profiles for each of the three HF components from

$$T_{MB}(\nu) = T_o \left(\frac{1}{e^{\frac{T_o}{T_{ex}}} - 1} - \frac{1}{e^{\frac{T_o}{2.73}} - 1} \right) (1 - e^{-\tau}), \quad (4)$$

where $T_{MB}(\nu)$ is the predicted brightness temperature, $T_o(\nu) = \frac{h\nu}{k}$, k is Boltzmann's constant, and h is Planck's constant (e.g., Mangum & Shirley 2015). The complete synthetic spectrum of the CN 2–1 lines for a given parameter set is obtained as the sum of intensities of the individual HF components, each of which are described by Eq. (4). This procedure was validated a posteriori because the excitation temperatures of each component

Table 3. Flux ratios for integrated spectra at radii >210 au.

HF component	Intensity ratio [b] (Theoretical)	West [a]			East [a]		
		Intensity ratio	*FHWM*	ΔV [c] km s^{-1}	Intensity ratio	*FHWM* km s^{-1}	ΔV [c]
A	0.6311	0.68 ± 0.05	0.40 ± 0.02	0.24 ± 0.01	0.54 ± 0.02	0.41 ± 0.01	0.25 ± 0.01
B	1	1	0.41 ± 0.01	0.25 ± 0.00	1	0.51 ± 0.01	0.31 ± 0.01
C	0.3755	0.47 ± 0.04	0.38 ± 0.02	0.23 ± 0.01	0.38 ± 0.02	0.47 ± 0.02	0.28 ± 0.01
D	0.1196	0.15 ± 0.04	0.33 ± 0.06	0.20 ± 0.03	0.17 ± 0.02	0.42 ± 0.03	0.25 ± 0.02
E	0.1189	0.10 ± 0.03	0.30 ± 0.08	0.18 ± 0.05	0.16 ± 0.02	0.40 ± 0.03	0.24 ± 0.02

Notes. [a]Values obtained from Gaussian fitting (see Sect. 3.2.2). [b]Theoretical ratio of intensities of HF transitions to the brightest HF transition ($J = 5/2 \rightarrow 3/2$, $F = 7/2 \rightarrow 5/2$). The relative intensities of the HF transitions of CN are adapted from Table 2 of Punzi et al. (2015). [c]$\Delta V = \frac{FWHM}{\sqrt{4 \ln 2}}$.

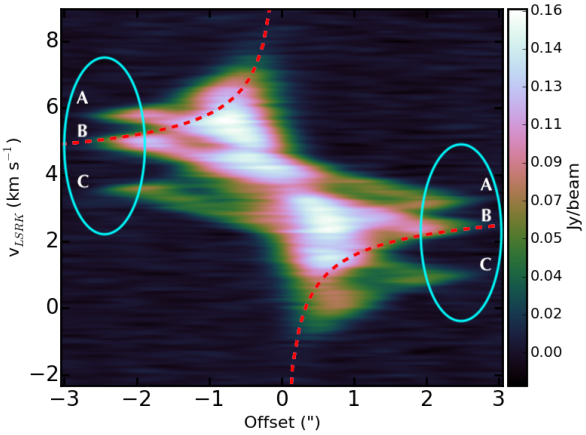

Fig. 4. Position-velocity diagram along the disk major axis of the CN emission. The dashed curve is a Keplerian velocity profile for a stellar mass of 0.61 $M_\odot$ at an inclination of 87°and a systemic velocity of 3.70 km s^{-1} LSRK. The $V_{\rm LSRK}$ scale is with respect to the brightest HF component (B) detected at frequency 226.8747813 GHz. Labels A, B, and C indicate the brightest HF transitions (see Table 1). Cyan ellipses correspond to the regions from which we extracted the spectra analyzed in Sect. 3.2.2.

are very similar and line overlap for the A and B components is modest (see Fig. 5). The set of synthetic spectra was then compared to the observed spectra using a χ^2 minimization process implemented in the PySpecKit Python package, which employs the Levenberg-Marquardt optimization method via the MPFIT algorithm (Markwardt 2009, and references within).

The preceding analysis was carried out for eight specific outer disk regions ($r > 210$ au) where the HF components are spectrally well resolved, on both the eastern and western sides of the disk (see Fig. 6 and Table 4). Figure 7 displays the CN spectra extracted from these eight regions – each with a diameter of one beamwidth (~0.6″), centered at upper and lower intermediate layers, midplane, and outer midplane, on both the eastern and western sides of the disk (Fig. 6) – overlaid with the best-fit LVG models (i.e., the model with the lowest χ^2 value). The values of $N_{\rm CN}$, $n_{\rm H_2}$, $T_{\rm kin}$, $T_{\rm ex}$, and τ obtained for each region from this χ^2 minimization process are listed in Table 4. We caution that – as is typical in such modeling – there is an inherent degeneracy, wherein the HF lines are well reproduced either by very dense and cold gas or by lower density, warmer gas.

These results (Table 4) indicate that the gas density traced by CN in the regions we modeled (Fig. 6) is a few times 10^6 cm^{-3} and that the gas is quite cold, with a best-fit $T_{\rm kin}$ in the range 10–12 K. We consistently find $T_{\rm ex} < T_{\rm kin}$, where $T_{\rm ex}/T_{\rm kin}$ decreases as $T_{\rm kin}$ increases, suggesting the gas may be somewhat sub-thermally excited. For $T_{\rm kin} > 25$ K, we find that the models fail to reproduce the intensity of the C component of the CN HF structure (they underestimate it). The best-fit CN column densities are consistently ~10^{13} cm^{-2}. The modeling results also indicate that the western side of the disk may be somewhat colder. We caution, however, that the results for $T_{\rm kin}$ are subject to systematic uncertainties (arising from, e.g., the various model assumptions and the specific approach to χ^2 minimization) that are difficult to quantify. The possibility of such an east-west asymmetry in the disk warrants follow-up via CN mapping at higher resolution.

4. Discussion

4.1. Vertical molecular emission structure

The analysis presented in Sect. 3.1 (see, in particular, Fig. 2) establishes that the CS, CN, and CO emission regions in the Flying Saucer disk are vertically stratified. To further demonstrate this vertical stratification, we have generated maps of the peak intensities of CN, CS, and CO (i.e., CASA "moment 8" maps) from their respective image cubes (presented in Figs. 3, B.1, and B.2). These peak emission images are rendered as a three-color (RGB) image in Fig. 8, where they are compared with a schematic illustration of the disk structure in these three tracers.

The structure illustrated in Fig. 8 can be summarized as follows: CO reaches the largest vertical extension, delineating the disk surface, with a deficit of CO near the midplane; CS emission is confined to the layers closest to the cold disk midplane; and CN traces the intermediate layers in between these extremes, albeit with some overlap with CS, in that the CN also appears to extend to near the midplane. As discussed in Dutrey et al. (2017), the midplane deficit of CO seems to correspond to the vertical settling of dust grains toward the midplane as traced by the 242 GHz continuum emission (Fig. 1d), which forms an elongated structure of about ~190 au in radius (see also Guilloteau et al. 2016). Of the three molecular tracers in the ALMA data thus far available for the Flying Saucer, it is evident from Figs. 2 and 8 that CS most closely traces this (vertically and radially confined) continuum emission, although CS is clearly more extended (in both dimensions). The CN originates from a layer that is radially more extended and more elevated with respect to CS. In addition, there appears to be a dearth of CN emission at the midplane at radii between ~80 and 200 au; this is apparent in the CN velocity channel maps (Fig. 3). At the outer

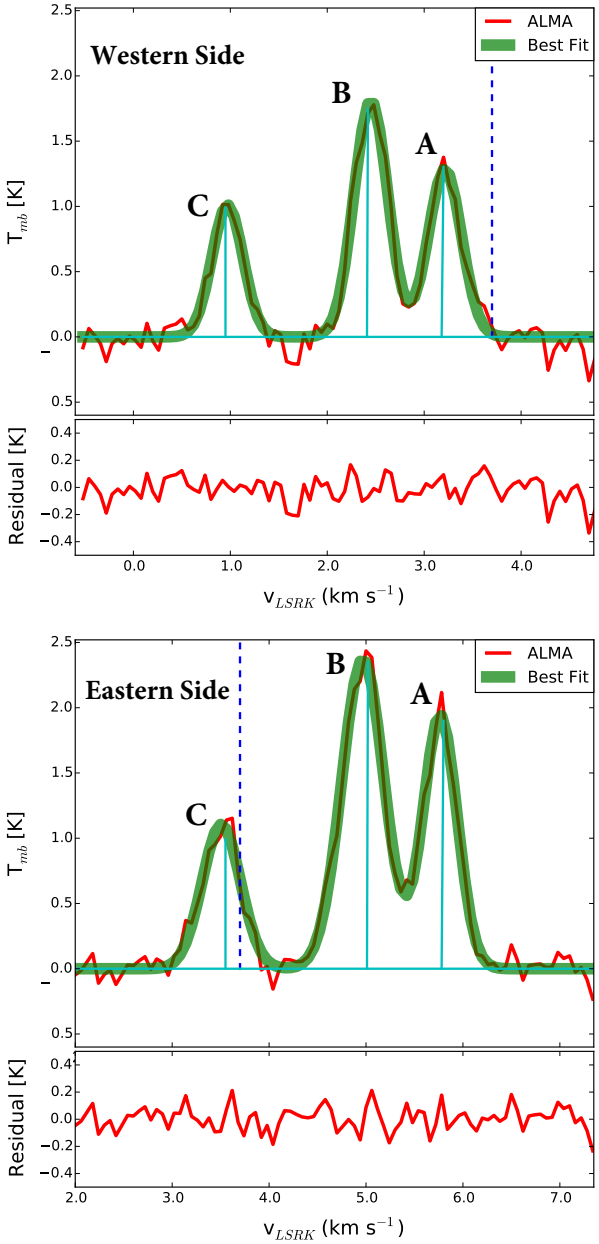

Fig. 5. Observed CN spectra (red), extracted from the outer region of the disk (>210 au), with the Gaussian fits (green). *Top and bottom panels*: HF structure extracted from the western and eastern sides of the disk, respectively. Cyan lines in the observed spectra mark the brightest HF components and have been scaled to match the peak intensity in the B component of the observed spectrum. The dashed blue line represents the systemic velocity of the system (~3.7 km s^{-1}). These data can be converted to Jy km s^{-1} by using the unit conversion factor of ~55 K.

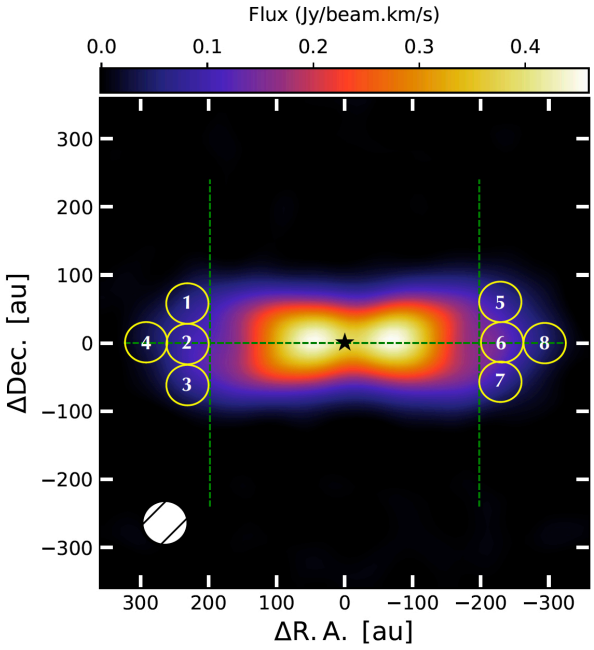

Fig. 6. Integrated intensity map of the CN emission overlaid with eight enumerated circles representing the eight single-beamwidth (0.3″ radius) regions from which we extract spectra at each side of the disk at radii > 210 au (see Table 4, Sect. 3.3, and Fig. 7). The synthesized beam size is indicated by the white ellipse. Vertical dashed green lines are placed at radii of ~210 au from the central star; the horizontal dashed green line indicates the disk midplane.

regions of the disk, the CN emission arises from the upper and lower intermediate layers and extends down to the midplane, outlining the disk radial extension. Possible mechanisms that might enhance CN production in these (intermediate) disk layers are discussed in Sect. 4.3.

Teague et al. (2016) previously suggested such a vertically stratified emission structure for CS, CN, and CO emission lines in the case of the nearly face-on TW Hydrae disk (TW Hya). From an analysis of multiple transitions of the three species, these investigators derived CO, CN, and CS excitation temperatures of ~35, 25, and 12 K, respectively (see also Teague & Loomis 2020). On this basis, Teague et al. (2016) deduced that the emission from the three molecules arises from decreasing heights above the disk midplane. This conclusion is consistent with the data presently available for the nearly edge-on Flying Saucer (Fig. 8), although we deduce colder excitation (and kinetic) temperatures for CN in this disk (see Sect. 4.3). However, the implied discrepancy in the thermal structures of the TW Hya and Flying Saucer disks is perhaps not surprising, given the different stellar parameters and ages of the two systems. In particular, the difference in the derived values of $T_{\rm kin}$ might lie with the fact that the TW Hya is a late-K star of rather advanced age (~8 Myr; e.g., Donaldson et al. 2016) and a luminous source of high-energy photons, with $L_{\rm X} = 1.4 \times 10^{30}$ ergs s^{-1} (Kastner et al. 2002), whereas the Flying Saucer's central star is a younger, M-type protostar that has thus far gone undetected in X-rays[4]. Furthermore, the TW Hya disk has a CN emission extension of ~180 au (Vlemmings et al. 2019; Teague & Loomis 2020), which is a factor of ~2 smaller than that of the Flying Saucer disk.

4.2. CN physical conditions

The results of our RADEX analysis indicate that the CN traces cold gas, and is optically thick, in the disk regions modeled via RADEX, namely, $T_{\rm kin}$ ~ 7–10 K (with total τ ~ 3–4) and $T_{\rm kin}$ ~ 8–12 K (with total τ ~ 3–5) at radii >210 au and heights <60 au on the western and eastern sides of the disk, respectively (Sect. 3.3). The low midplane temperatures appear compatible

[4] *Chandra* and *XMM-Newton* X-ray observations of a ρ Oph field that included the Flying Saucer were obtained in 2000 and 2003 with exposure times of ~5 and ~34 ks, respectively. Neither observation yields a detection at the position of the object. Given the disk's edge-on orientation, however, it is difficult to draw conclusions as to the intrinsic X-ray luminosity of the central star.

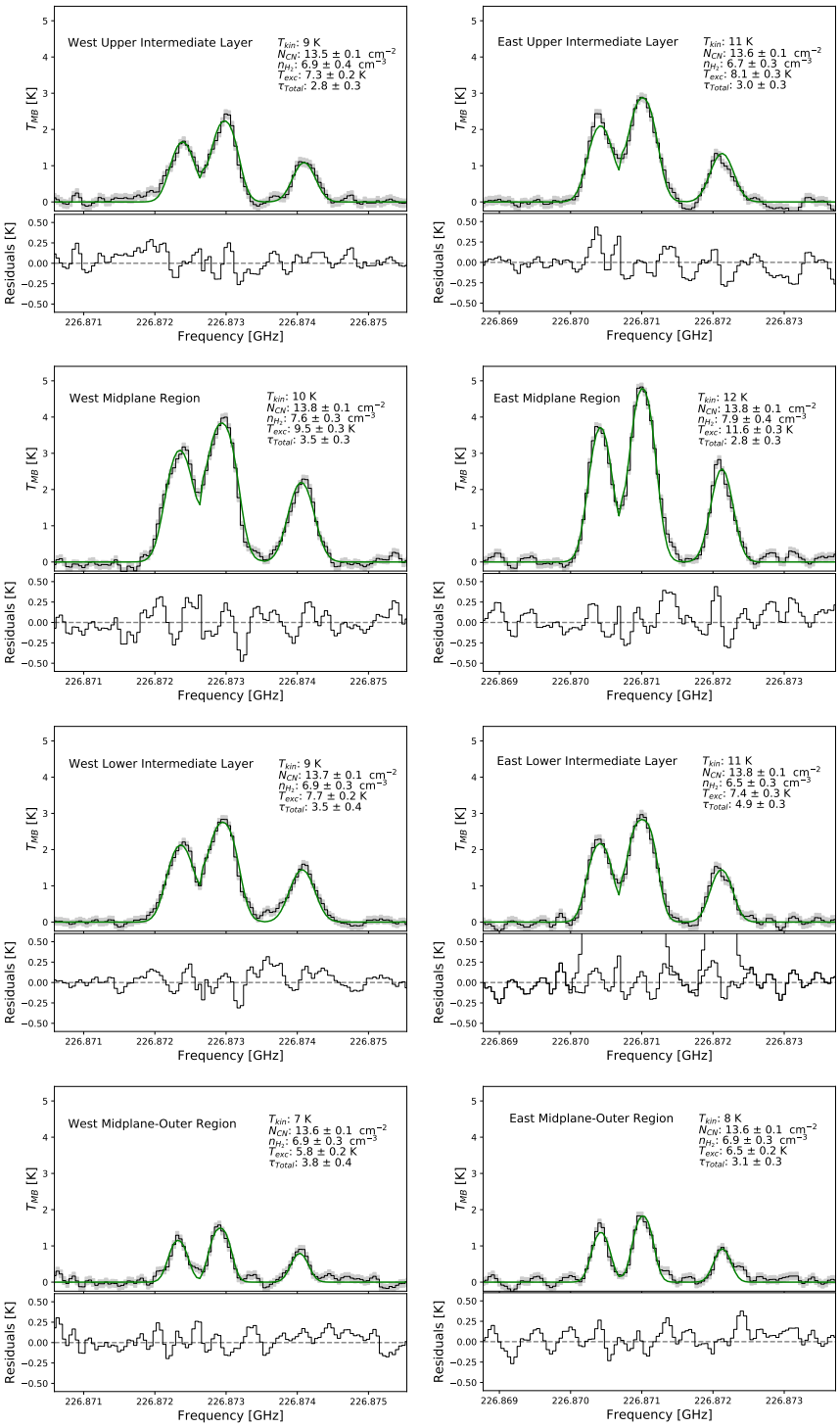

Fig. 7. Spectra of the integrated CN (2–1) emission from the upper intermediate layers, lower intermediate layers, midplane, and outer midplane regions of the disk along with the simultaneous fits to components A, B, and C (see Table 3). The best-fit LVG models from the χ^2 minimization are displayed as a green line. The fitted parameters are the total optical depth (τ; A+B+C), excitation temperature ($T_{\rm ex}$), and, on a logarithmic scale, CN column density ($N_{\rm CN}$) and particle density ($n_{\rm H_2}$; see Table 4). Spectra in the left and right columns are extracted from the western and eastern sides of the disk, respectively. The fit residuals are shown as a function of frequency at the bottom of each panel. The shaded gray area shows the error computed from a signal-free part of the spectra.

with a model of the temperature structure of the Flying Saucer disk obtained by Dutrey et al. (2017) from numerical simulations of the disk's CO emission. Specifically, those authors found $T \sim 5$–10 K in the disk midplane at offsets of ~230–280 au (Dutrey et al. 2017, their Fig. 8g), corresponding to the western and eastern midplane regions we included in our analysis (Table 4). Furthermore, the densities we obtained from our line profile modeling (~10^6 to 10^7 cm^{-3}; Table 4) are generally consistent with, if somewhat smaller than, the densities predicted for these same (external) disk regions in the Dutrey et al. (2017) modeling (their Fig. 7). Their modeling also indicates, however, that $T_{\rm kin} \sim 15$–25 K at heights of ~50 au at the same radial offsets (~230–280 au). These disk regions correspond to the "intermediate layers" for which we find $T_{\rm kin} \sim 9$–11 K based on RADEX line profile fitting (Table 4), and they are not significantly different from the corresponding values in the midplane. This lack of a significant vertical gradient in $T_{\rm kin}$ at radii >210 au, as inferred from CN emission, may indicate that the standard protoplanetary disk model, on which the Dutrey et al. (2017) modeling is based, may not describe the vertical temperature structure in the Flying Saucer well.

On the other hand, our RADEX modeling also yields evidence that the CN molecules are sub-thermally excited ($T_{\rm ex} < T_{\rm kin}$) away from the midplane, with the divergence between

Table 4. RADEX model parameters.

No.	Region	Location		T_{kin}	n_{H_2}	N_{CN}	T_{ex}	τ [a]
		Δ RA [au]	Δ Dec [au]	[K]	$\times 10^6$ [cm^{-3}]	$\times 10^{13}$ [cm^{-2}]	[K]	
1.	W. upper intermediate layer	+230	+50	9	6.8	3.5	7.3	2.8
2.	W. midplane	+ 230	+0.0	10	50.0	6.0	9.5	3.5
3.	W. lower intermediate layer	+230	−50	9	8.0	4.4	7.7	3.5
4.	W. outer midplane	+280	+0.0	7	7.3	4.2	5.8	3.8
5.	E. upper intermediate layer	−230	+50	11	5.4	3.9	8.1	3.0
6.	E. midplane	−230	+0.0	12	74.0	5.7	11.6	2.8
7.	E. lower intermediate layer	−230	−50	11	3.2	6.4	7.4	4.9
8.	E. outer midplane	−280	+0.0	8	7.0	3.7	6.5	3.1

Notes. [a] Sum of the opacities at the line center of the A, B, and C HF components.

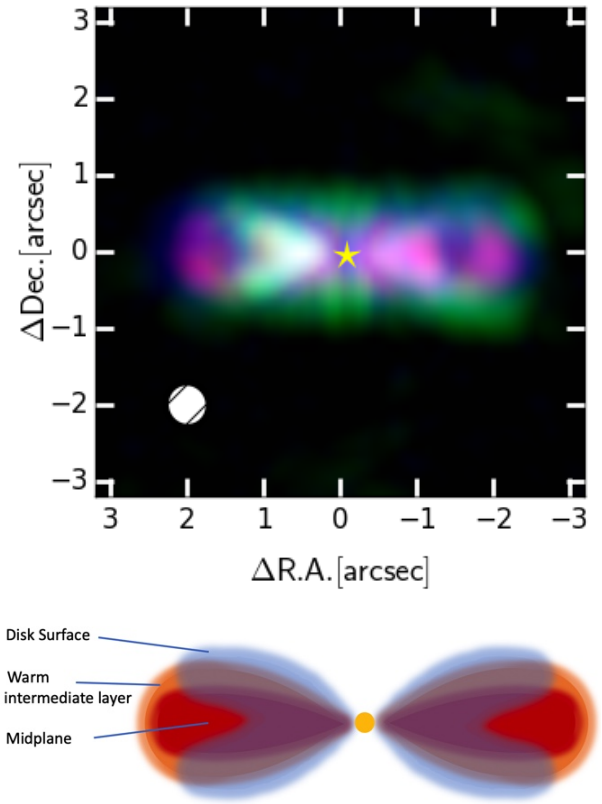

Fig. 8. Comparison of CS, CN, and CO emission using peak intensity (CASA moment 8) maps. *Top*: RGB image generated from CS, CN, and CO peak intensity maps. CS, CN, and CO are assigned to the red, green, and blue channels, respectively; each color channel is scaled linearly. *Bottom*: schematic illustration of the different layers traced by CS (midplane), CN (midplane to intermediate layers), and CO (upper disk surface) emission.

T_{ex} and T_{kin} more evident on the eastern side of the disk (Table 4). We caution that, as noted earlier, it remains to be determined whether the apparent differences in the CN thermalization inferred for the two sides of the disk reflect a real asymmetry in the disk's physical conditions. Indeed, one difficulty with the low T_{kin} inferred here is that one would expect CN and CS to be severely depleted from the gas phase in disk regions in which T_{kin} drops well below the freeze-out temperature of CO (i.e., ∼17–19 K). However, sub-thermal excitation becomes more likely in disk regions with a significant degree of depletion of dust grains, which may characterize the Flying Saucer at radii >210 au. Previous studies have shown that when the gas-to-dust ratio drops to ∼20 (or n_{H_2} drops by a factor of ∼5), CN would be produced under sub-thermal excitation conditions, although this is only expected in regions where the density is on the order of a few 10^5 cm^{-3} (Chapillon et al. 2012).

4.3. CN: location and formation

Cazzoletti et al. (2018) modeled CN emission from protoplanetary disks under the assumption that CN formation mainly proceeds through the far ultraviolet (FUV) pumping of H_2 to vibrationally excited levels, in addition to the photodissociation of HCN. As a main result, the highest CN abundance should be located in the upper region of the disk, while the emission extends down to the midplane in outer disk regions, forming a CN emission ring. Although the HF transitions are not specifically considered in this model, the CN features observed in the Flying Saucer disk appear reasonably consistent with the predicted formation pathway, where CN is produced near the surface and outer regions of the disk (Fig. 3). However, it is apparent from Fig. 2 that the CN layer lies between the CO and CS layers, clearly showing that CN emission traces intermediate layers rather than disk surface layers. In addition, the strong link between UV radiation and CN formation would appear to require that most of the CN emission arise from upper disk layers, given that the FUV radiation field is attenuated by dust at moderate disk depths (Gorti et al. 2009). Indeed, the notion that UV controls the abundance of CN is consistent with the deficit of midplane CN emission at radii between ∼80 and 200 au (see Fig. 3), matching the spatial extension of the 242 GHz continuum.

However, as noted earlier, we also find that the CN arises from very cold ($T_{kin} \lesssim 15$ K) regions of the disk (Sect. 4.2). This suggests that FUV radiation alone may be insufficient to explain the observed CN abundances, and one must invoke more deeply penetrating sources of high-energy radiation, such as X-rays (see discussions in Kastner et al. 2014; Hily-Blant et al. 2017). Indeed, the bulk of the CN intensity is localized within the central ∼0.8″ (∼100 au) radius (Fig. 1b) of the disk, a region where enhancement of CN production can be generated by exposing a disk that is in advanced stages of settling to X-rays or a combination of X-rays and FUV radiation (Stäuber et al. 2005, 2007). Moreover, recent simulations from detailed physical and chemical disk models indicate that the distribution of radicals such as

CN could be present as multilayered structures (e.g., Ruaud & Gorti 2019). In fact, several channel maps of the CN line (Fig. 3) appear to show emission arising from the midplane, especially at the inner part of the CN emission "ring", while there are velocities in the channel maps at which it appears that CN arises from intermediate layers at larger disk radii. These structures are qualitatively similar to the predictions of the Ruaud & Gorti (2019) models. Both emission regions may contribute to low-temperature CN emission, such as we infer from our RADEX modeling (Sect. 3.3). Higher-resolution ALMA imaging spectroscopy of multiple transitions of CN would help establish whether there are indeed two distinct disk layers involved in efficient CN production.

5. Summary

Using archival ALMA data, we have investigated the vertical chemical and physical structure of the edge-on Flying Saucer disk. This is in order to constrain CN formation pathways that took place during disk evolution and planetary formation. In particular, we used RADEX models to generate CN (2–1) synthetic spectra and thus predict the disk thermal conditions that characterize the observed CN emission from the Flying Saucer disk. As a comparative approach, we used molecular lines tracing different disk physical conditions, specifically ^{12}CO and CS, in order to further spatially constrain the location of the CN emission. Our main results are as follows:

- We demonstrate that ^{12}CO, CN, and CS molecular lines can be used to trace the vertical structure of edge-on disks. We estimated the scale heights of these molecules, and they reveal a stratified structure within the flared Flying Saucer disk. Basically, ^{12}CO traces the low-density disk surface, while CN and CS trace the denser intermediate layers and midplane region, respectively.
- The analysis of the CN channel maps reveals complex structures superimposed on the Keplerian gas kinematics of the Flying Saucer disk. An outstanding feature is the CN emission deficit near the midplane at radii >100 au, predominantly arising from intermediate layers. However, in the inner regions of the disk, CN emission appears to arise from layers closer to the midplane. This variation of the CN vertical location along the disk might be related to the formation route of CN, whose production is likely related to the degree of irradiation of the flared disk by X-rays and UV photons from the central star.
- Based on RADEX non-LTE modeling of the three brightest HF components of the CN(2–1) line, we estimated thermal parameters in different regions of the disk. Our results characterized a disk with thermal emission from the midplane and sub-thermal conditions in intermediate layers. Near the disk midplane, where we derive densities of $n_{\rm H_2} \sim 10^7$ cm^{-3} at relatively low $T_{\rm kin}$ (∼12 K), we find that CN is thermalized, while sub-thermal non-LTE conditions appear to be obtained for CN emission from higher (intermediate) disk layers.
- Higher-resolution ALMA imaging spectroscopy of multiple transitions of CN is required to confirm the cold outer disk temperatures we infer from our radiative transfer modeling. Such follow-up observations would also help establish whether there exist multiple, distinct disk layers involved in efficient CN production.

As demonstrated here, species with different critical densities can trace temperature and density gradients across the radial and vertical structures of protoplanetary disks. However, higher spatial resolution observations of multiple transitions are required to distinguish and estimate with higher accuracy the thermal conditions needed for producing the distinct chemical abundances from which planets form.

Acknowledgements. We wish to thank the anonymous referee for providing insightful comments. This research is supported by NASA Exoplanets Program grant 80NSSC19K0292 to Rochester Institute of Technology. This paper makes use of the following ALMA data: ADS/JAO.ALMA#2013.1.00387.S. ALMA is a partnership of ESO (representing its member states), NSF (USA) and NINS (Japan), together with NRC (Canada), MOST and ASIAA (Taiwan), and KASI (Republic of Korea), in cooperation with the Republic of Chile. The Joint ALMA Observatory is operated by ESO, AUI/NRAO and NAOJ. The National Radio Astronomy Observatory is a facility of the National Science Foundation operated under cooperative agreement by Associated Universities, Inc.

References

Bergner, J. B., Guzmán, V. G., Öberg, K. I., Loomis, R. A., & Pegues, J. 2018, ApJ, 857, 69
Cazzoletti, P., van Dishoeck, E. F., Visser, R., Facchini, S., & Bruderer, S. 2018, A&A, 609, A93
Chapillon, E., Guilloteau, S., Dutrey, A., Piétu, V., & Guélin, M. 2012, A&A, 537, A60
Cleeves, L. I., Adams, F. C., & Bergin, E. A. 2013, ApJ, 772, 5
Donaldson, J. K., Weinberger, A. J., Gagné, J., et al. 2016, ApJ, 833, 95
Dutrey, A., Guilloteau, S., Piétu, V., et al. 2017, A&A, 607, A130
Gaia Collaboration (Brown, A. G. A., et al.) 2018, A&A, 616, A1
Ginsburg, A., & Mirocha, J. 2011, PySpecKit: Python Spectroscopic Toolkit
Gorti, U., Dullemond, C. P., & Hollenbach, D. 2009, ApJ, 705, 1237
Grosso, N., Alves, J., Wood, K., et al. 2003, ApJ, 586, 296
Guilloteau, S., Simon, M., Piétu, V., et al. 2014, A&A, 567, A117
Guilloteau, S., Piétu, V., Chapillon, E., et al. 2016, A&A, 586, L1
Guzmán, V. V., Öberg, K. I., Huang, J., Loomis, R., & Qi, C. 2017, ApJ, 836, 30
Hily-Blant, P., Pineau des Forêts, G., Faure, A., Le Gal, R., & Padovani, M. 2013, A&A, 557, A65
Hily-Blant, P., Magalhaes, V., Kastner, J., et al. 2017, A&A, 603, L6
Hily-Blant, P., Magalhaes de Souza, V., Kastner, J., & Forveille, T. 2019, A&A, 632, L12
Kastner, J. H., Zuckerman, B., Weintraub, D. A., & Forveille, T. 1997, Science, 277, 67
Kastner, J. H., Huenemoerder, D. P., Schulz, N. S., Canizares, C. R., & Weintraub, D. A. 2002, ApJ, 567, 434
Kastner, J. H., Zuckerman, B., & Bessell, M. 2008, A&A, 491, 829
Kastner, J. H., Hily-Blant, P., Rodriguez, D. R., Punzi, K., & Forveille, T. 2014, ApJ, 793, 55
Kastner, J. H., Qi, C., Dickson-Vandervelde, D. A., et al. 2018, ApJ, 863, 106
Lepp, S., & Dalgarno, A. 1996, A&A, 306, L21
Loinard, L., Torres, R. M., Mioduszewski, A. J., & Rodríguez, L. F. 2008, ApJ, 675, L29
Mangum, J. G., & Shirley, Y. L. 2015, PASP, 127, 266
Markwardt, C. B. 2009, ASP Conf. Ser., 411, 251
Öberg, K. I., & Wordsworth, R. 2019, AJ, 158, 194
Öberg, K. I., Guzmán, V. V., Furuya, K., et al. 2015, Nature, 520, 198
Punzi, K. M., Hily-Blant, P., Kastner, J. H., Sacco, G. G., & Forveille, T. 2015, ApJ, 805, 147
Qi, C., Öberg, K. I., Wilner, D. J., et al. 2013, Science, 341, 630
Qi, C., Öberg, K. I., Espaillat, C. C., et al. 2019, ApJ, 882, 160
Reboussin, L., Guilloteau, S., Simon, M., et al. 2015, A&A, 578, A31
Ruaud, M., & Gorti, U. 2019, ApJ, 885, 146
Sacco, G. G., Kastner, J. H., Forveille, T., et al. 2014, A&A, 561, A42
Semenov, D., Favre, C., Fedele, D., et al. 2018, A&A, 617, A28
Skatrud, D. D., de Lucia, F. C., Blake, G. A., & Sastry, K. V. L. N. 1983, J. Mol. Spectr., 99, 35
Stäuber, P., Doty, S. D., van Dishoeck, E. F., & Benz, A. O. 2005, A&A, 440, 949
Stäuber, P., Benz, A. O., Jørgensen, J. K., et al. 2007, A&A, 466, 977
Teague, R., & Loomis, R. 2020, ApJ, 899, 157
Teague, R., Guilloteau, S., Semenov, D., et al. 2016, A&A, 592, A49
Thi, W., van Zadelhoff, G., & van Dishoeck, E. F. 2004, A&A, 425, 955
van der Tak, F. F. S., Black, J. H., Schöier, F. L., Jansen, D. J., & van Dishoeck, E. F. 2007, A&A, 468, 627
van Terwisga, S. E., van Dishoeck, E. F., Cazzoletti, P., et al. 2019, A&A 623, A150
Visser, R., Bruderer, S., Cazzoletti, P., et al. 2018, A&A, 615, A75
Vlemmings, W. H. T., Lankhaar, B., Cazzoletti, P., et al. 2019, A&A, 624, L7
Weaver, E., Isella, A., & Boehler, Y. 2018, ApJ, 853, 113

Appendix A: CN HF components

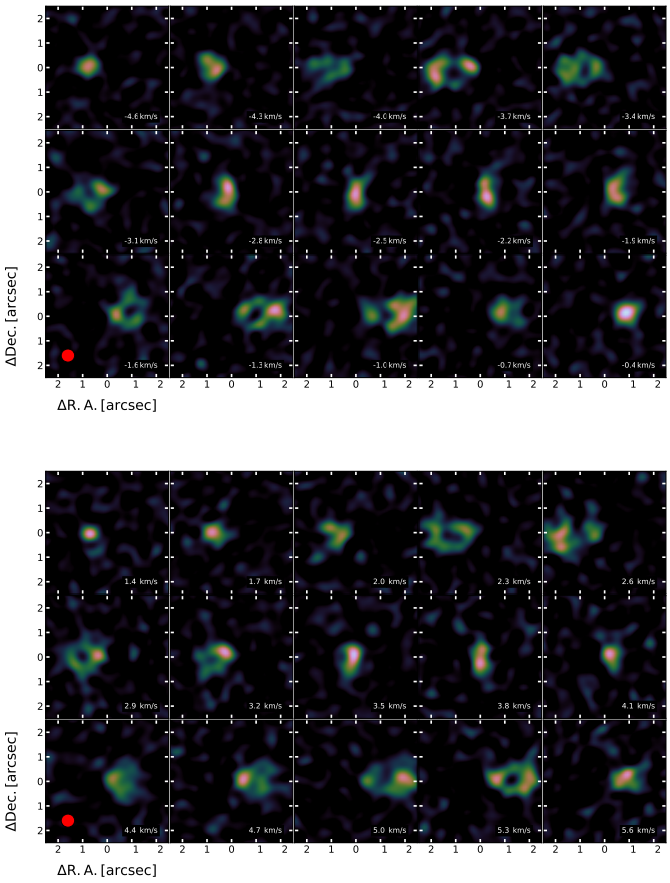

Fig. A.1. Channel maps of the CN emission in the Flying Saucer from −4.60 to −0.40 km $^{-1}$ and from 1.40 to 5.60 km $^{-1}$. The frequency range is presented for the D (*top*) and E (*bottom*) HF components, which are $J = 5/2 \rightarrow 3/2$, $F = 3/2 \rightarrow 3/2$ and $J = 5/2 \rightarrow 3/2$, $F = 5/2 \rightarrow 5/2$, respectively (see Table 3). The spectral resolution is 0.3 km s^{-1} and the rms per channel is 2.9 mJy beam^{-1}. The synthesized beam size is represented in the *lower left panel*.

The CN $N = (2–1)$ HF component channel maps of the C and D components are displayed in Fig. A.1. These satellite components also present a typical Keplerian rotation in a disk. In Fig. A.2, we present PV diagrams along the disk's major axis overlaid with curves representing Keplerian rotation in a geometrically thin disk with an inclination of 87 ± 1.0 deg, a central mass of 0.60 ± 0.02 $M_\odot$, and a $v_{\rm LSRK}$ of 3.70 ± 0.5 km s^{-1}, assuming a distance of 120 pc.

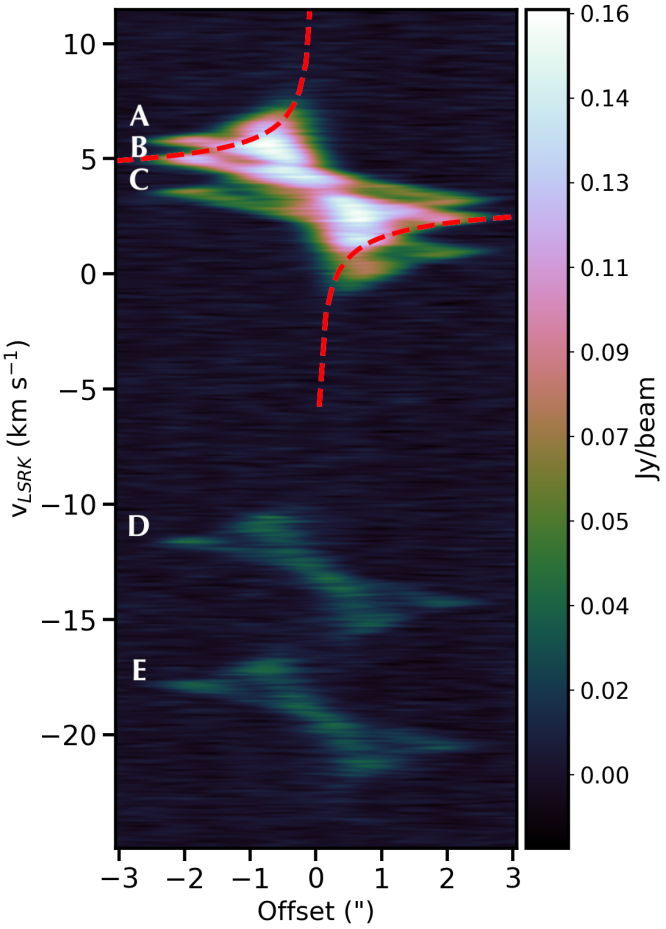

Fig. A.2. Position-velocity diagram of the CN emission along the disk's major axis. The dashed curve is a Keplerian velocity profile for a stellar mass of 0.61 $M_\odot$ at an inclination of 87° and a systemic velocity of 3.70 km s^{-1} LSRK. Labels A, B, C, D, and E indicate the five observed HF transitions (see Table 3).

Appendix B: CS and CO emission: channel maps

Channel maps of CS and CO toward the Flying Saucer disk are displayed in Figs. B.1 and B.2. For a direct comparison, the velocity range is similar to those of the channel maps for CN presented in Fig. 3.

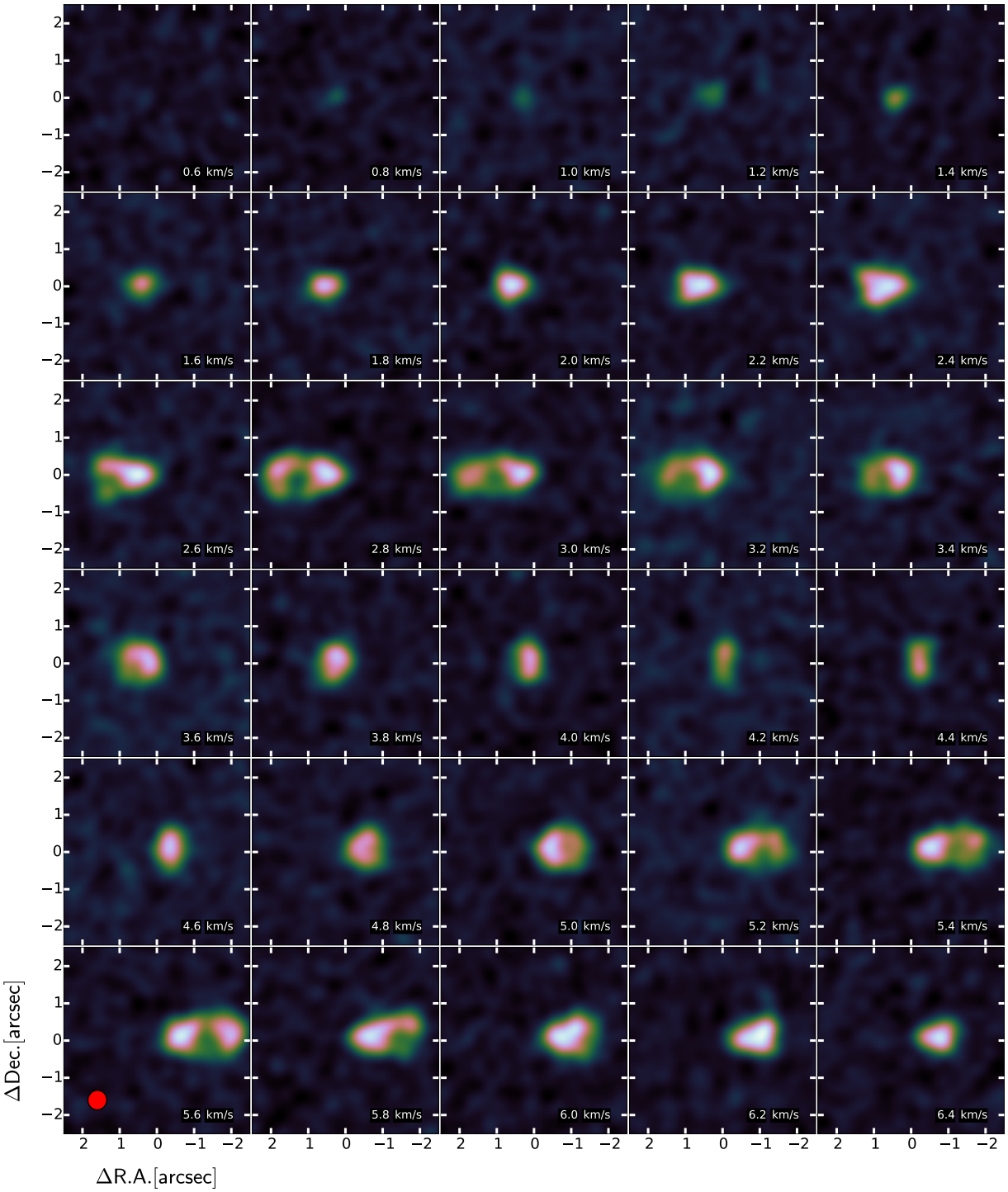

Fig. B.1. Channel maps of the CS emission in the Flying Saucer from 0.60 to 6.40 km s^{-1}. The spectral resolution is 0.2 km s^{-1} and the rms per channel is 3.0 mJy beam^{-1}. The synthesized beam size is represented in the *lower left panel*.

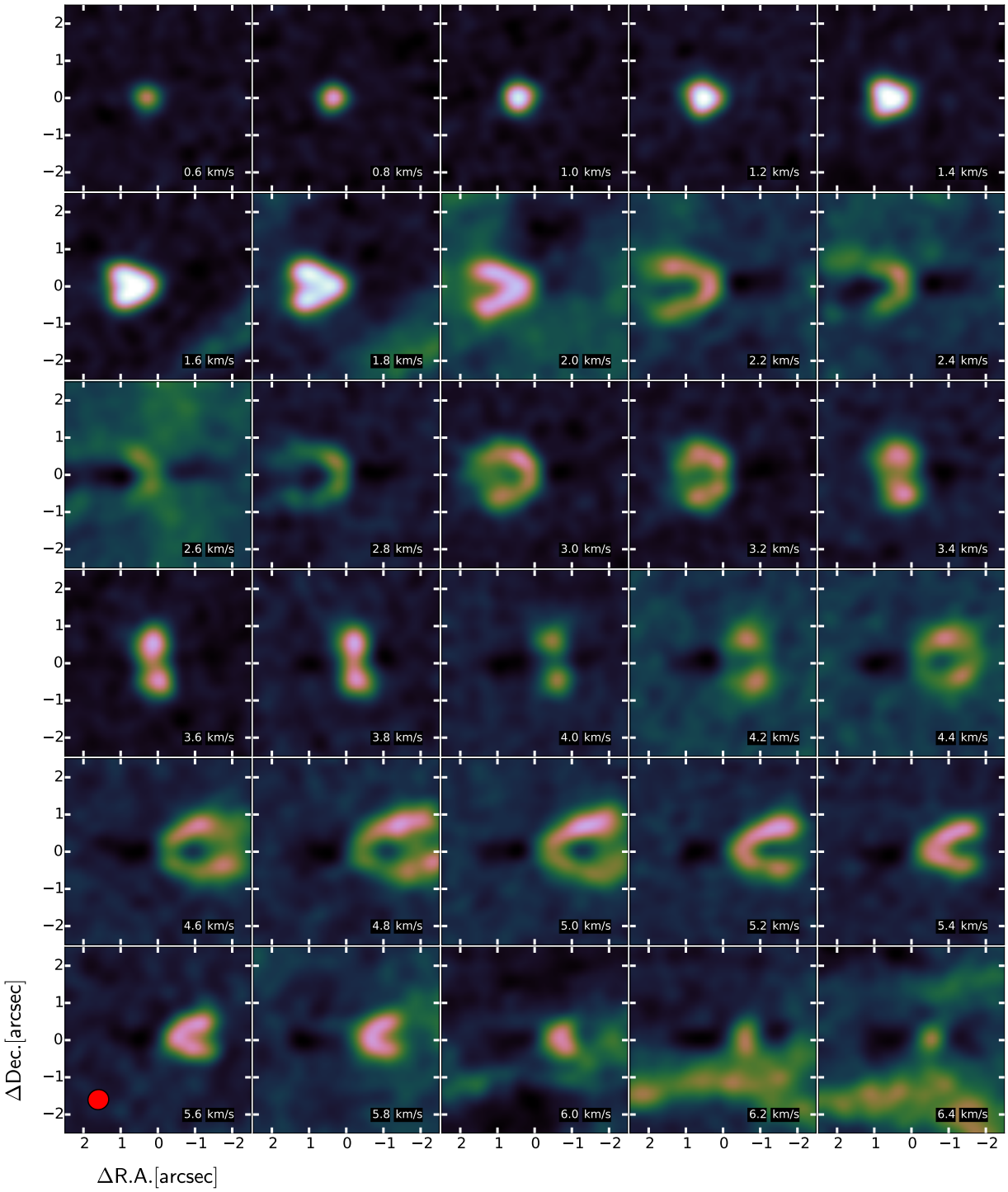

Fig. B.2. Channel maps of the CO emission in the Flying Saucer from 0.60 to 6.40 km s^{-1}. The spectral resolution is 0.2 km s^{-1} and the rms per channel is 5.0 mJy beam^{-1}. The synthesized beam size is represented in the *lower left panel*.